Journal of Geochemical Exploration 253 (2023) 107281

Contents lists available at ScienceDirect

Journal of Geochemical Exploration

journal homepage: www.elsevier.com/locate/gexplo

The origin and ore-forming processes of the Qixiashan Pb–Zn–Ag deposit, South China: Constraints from LA–ICP–MS analysis of pyrite and sphalerite

Haotian Gong [a,b], Youqiang Qi [a,*], Jianfeng Gao [a], Chuan Lv [a,b], Kang Min [a,b], Tingguang Lan [a]

[a] State Key Laboratory of Ore Deposit Geochemistry, Institute of Geochemistry, Chinese Academy of Sciences, Guiyang 550081, China
[b] University of Chinese Academy of Sciences, Beijing 100049, China

ARTICLE INFO

Keywords:
Qixiashan Pb–Zn–Ag deposit
Sulfide minerals
Minor and trace elements
Ore-forming fluid evolution

ABSTRACT

The Qixiashan Pb–Zn–Ag deposit, located in the Nanjing–Zhenjiang area of the Middle–Lower Yangtze Metallogenic Belt (MLYB), is one of the largest Pb—Zn deposits in Eastern China. The middle Carboniferous carbonates of the Huanglong Formation are the main host rocks of orebodies. Whether this deposit is associated with magmatic activity or sedimentary exhalative deposit is still debated due to the poor constraints on the origin of the ore materials and metallogenic processes. To address this, we analyzed the compositions of pyrite and sphalerite from different mineralization stages and depths, and the distributions of minor and trace elements within the pyrite and sphalerite crystals, using in situ laser ablation–inductively coupled plasma–mass spectrometer and scanning electron microscope analyses. Four hydrothermal stages can be identified: the pre-ore pyrite stage (stage I); Pb–Zn–Py stage (stage II); Pb–Zn–Ag stage (stage III); and carbonate stage (stage IV). The sphalerite in the deposit is typically enriched in Fe, Mn, In, and Sn, and depleted in Ge and Cd. These results are characteristic of magmatic hydrothermal activity and indicate the mineralization was related to late Yanshanian magmatic activity. The Co and Ni contents of pyrite, and the Fe, In, and Sn contents of sphalerite decrease from the early to late stages, suggesting that the temperature of the hydrothermal fluid decreased continuously. Variations in the Se content of pyrite suggest that the fO_2 increased from stage I to stage II, then decreased during stage III. Detailed SEM and elemental maps show that stage-II sphalerite (Sph-1) and pyrite (Py-2) are oscillatory zoned, which we interpret to reflect pressure fluctuations and repeated local fluid phase separation during stage II. We also infer from the zoning and subsequent formation of Py-3 that magmatic hydrothermal activity increased from stage I to II, then decreased from stage II to III. In addition, changes in the In, Sn, and Fe contents of sphalerite can be useful indicators of the upward migration of ore-forming fluid and can help during prospecting for related deep magmatic rocks.

1. Introduction

Magmatic hydrothermal metallogenic systems hosted in carbonate rocks are normally characterized by central intrusive rocks surrounded by continuous alteration zones (Einaudi et al., 1981). Due to variations in physicochemical conditions (e.g., temperature, pressure, oxygen fugacity and sulfur fugacity), ore-forming elements (e.g., Cu, Mo, Fe, Ag, W, Sn, Au, Pb, Zn) are often zoned with different spatial patterns from the magmatic source, which leads to the formation of economic deposits (Meinert, 1987; Hedenquist and Lowenstern, 1994; Fournier, 1999; Sillitoe, 2010; Mao et al., 2011a, 2013). These systems are distributed widely across the globe, including proximal W—Sn skarn and distal Pb—Zn veins at Menheniot and Porthleven in Cornwall, UK (Wilkinson et al., 2000), and proximal W–Sn–Mo–Bi skarn and distal Pb–Zn–Ag veins in Shizhuyuan, China (Wu, 2016). Lead, Zn and Ag mineralization is often located far from the magmatic source in magmatic hydrothermal systems. Furthermore, when Pb–Zn–Ag deposits are not directly in contact with intrusions and some orebodies are stratiform or stratabound, it is difficult to distinguish their genetic type and understand the metallogenic process (Baker et al., 2004; Williams-Jones et al., 2010; Mao et al., 2011b; Wu et al., 2015).

The Qixiashan Pb–Zn–Ag deposit, located in the Nanjing-Zhenjiang region of the Middle–Lower Yangtze River Polymetallic Metallogenic Belt (MLYB) in the South China Block, is a typical carbonate-hosted deposit. It contains >260 million tons of Pb—Zn resources with average grades of 4.57 % Pb and 7.49 % Zn, along with exploitable Mn

* Corresponding author.
E-mail address: qiyouqiang@mail.gyig.ac.cn (Y. Qi).

https://doi.org/10.1016/j.gexplo.2023.107281
Received 8 May 2022; Received in revised form 10 June 2023; Accepted 26 July 2023
Available online 1 August 2023

and Ag (Sun et al., 2018, 2020). The deposit is hosted primarily in carbonates of the Huanglong Formation and is not in contact with magmatic rocks. In recent decades, many studies of the deposit have been conducted, including geophysical and geochemical prospecting (Wang and Zhou, 1993; Liu, 1999), fluid inclusions studies (Xie and Yin, 1997; Gui, 2012; Sun et al., 2018), and isotope geochemistry studies (Xu and Zeng, 2006; Zhang et al., 2017, 2019; Sun et al., 2018; Gong et al., 2020). However, there is debate over the genesis of this deposit and the ore-forming process. Several genetic models have been proposed, including sedimentary-exhalative (SEDEX) (e.g., Gui, 2012), magmatic hydrothermal activity (e.g., Zhang, 2015; Zhang et al., 2017; Gong et al., 2020) and synsedimentary deposition followed by hydrothermal overprinting (e.g., Sun et al., 2018, 2020).

Pyrite and sphalerite are common ore minerals in the Qixiashan deposit, and formed throughout the metallogenesis. They can incorporate appreciable amounts of minor and trace elements (e.g., Co, Ni, Mn, In, Ag, Se). Pyrite and sphalerite compositional data are valuable petrogenetic tools to classify the genesis of ore deposits and trace the mineralization processes (Huston et al., 1995; Fernández et al., 2000; Di Benedetto et al., 2005; Gottesmann and Kampe, 2007; Cook et al., 2009; Large et al., 2009; Wang et al., 2010; Ye et al., 2011; Lockington et al., 2014; George et al., 2015; Qi et al., 2022). Furthermore, much progress in ore prospecting for deep deposits has been achieved in recent years (e.g., borehole KK4603 in line 46, 625–1010 m deep). Here, we focus on pyrite and sphalerite, using the scanning electron microscope (SEM) and laser ablation–inductively coupled plasma–mass spectrometer (LA–ICP–MS) to determine the origin of the ore material and the ore-forming process that occurred in the Qixiashan polymetallic deposit.

2. Regional geology

The Nanjing-Zhenjiang region, in the east of the fault depression zone on the northern margin of the Yangtze block, is an important part of the Fe–Cu–Pb–Zn polymetallic metallogenic belt in the MLYB (Fig. 1). There are four main ore-hosting strata in this region: the base of the Carboniferous Huanglong Formation (limestone), the Gaolishan Formation (sandstone, siltstone), the top of the Permian Qixia Formation (limestone), and the top of the Triassic Qinglong Formation (limestone).

The Nanjing–Zhenjiang region has experienced three major tectonic events since the Proterozoic. Marine sediments and volcanic rocks in Proterozoic were deformed and metamorphosed during the Jinning Orogeny, producing Neoproterozoic basement consisting of schist, slate, and metavolcanics. From the Silurian to the middle Triassic, crustal evolution was dominated by the deposition of a 7700 m-thick sequence of marine carbonate, continental siltstone and shale. During the Indosinian Orogeny, the region underwent N—S compression and the regional rocks were strongly deformed and uplifted with intense folding. This formed three anticlines and two synclines with E–W-striking axes. Due to the northwestward subduction of the paleo-Pacific Plate beneath the South China Block, intense faulting occurred during the Yanshanian, causing the development of N—S trending faults and multistage magmatic intrusions. The Yanshanian was the period of most intense magmatic activity in this area, from 145 to 65 Ma (Zhang, 2015; Sun et al., 2018; Wei et al., 2019).

Regional intrusive rocks covering an area of ~700 km^2 are extensive (Fig. 2). Intermediate–mafic, intermediate–felsic, and felsic rock assemblages were successively formed, from west to east, accounting for about 80 % of the exposed intrusive rocks by area (Mao and Zhao, 1990). A series of ore deposits, including the Qixiashan Pb–Zn–Ag, the Anjishan Cu, the Funiushan Cu, the Tongshan Cu—Mo, and the Weigang Fe, have been found in this region. It is thought that these endogenous polymetallic deposits are related to the late Yanshanian magmatic activity (e.g., Sun et al., 2014; Zeng et al., 2013; Wang et al., 2014; Zhang, 2015; Guan et al., 2015; Zhou et al., 2016).

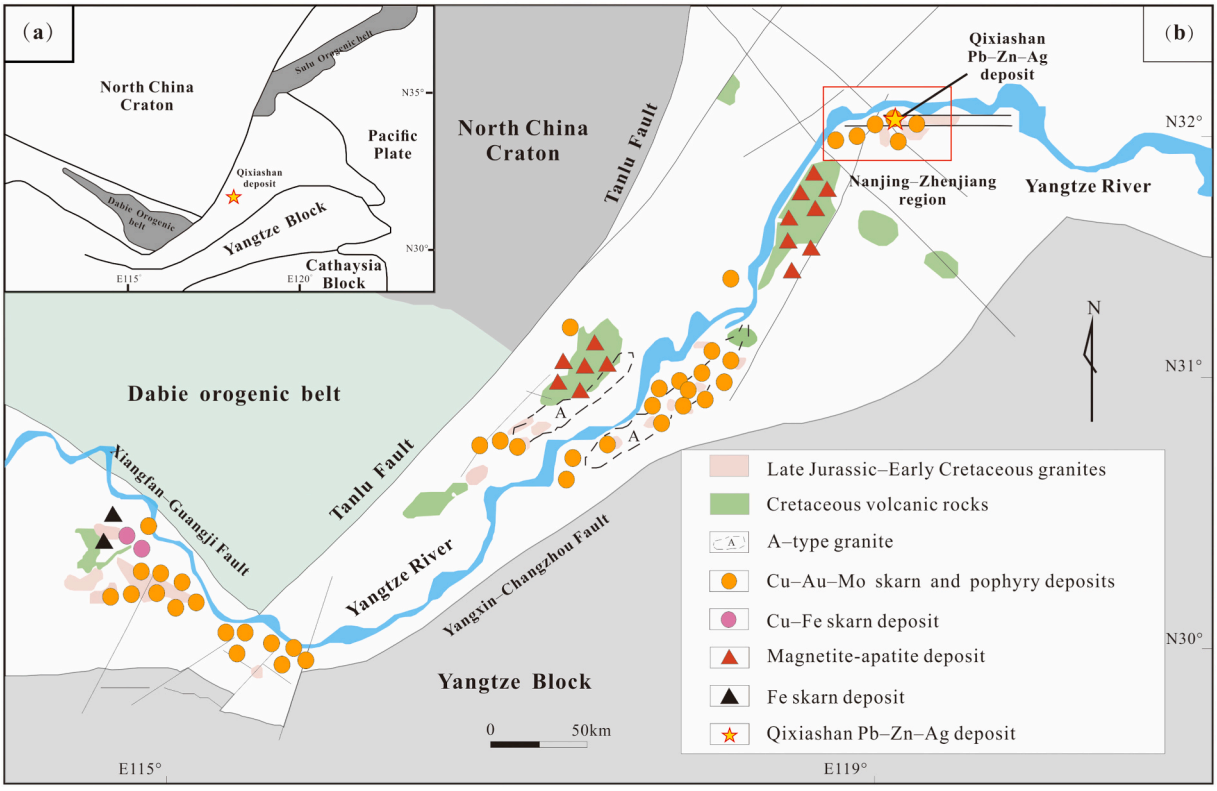

Fig. 1. (a) Sketch map of the major tectonic units of eastern China and (b) the distribution of Mesozoic magmatic rocks associated with Cu–Au–Fe deposits in the Middle–Lower Yangtze River Valley Metallogenic Belt (modified from Mao et al., 2006; Wang et al., 2014; Zhang et al., 2017).

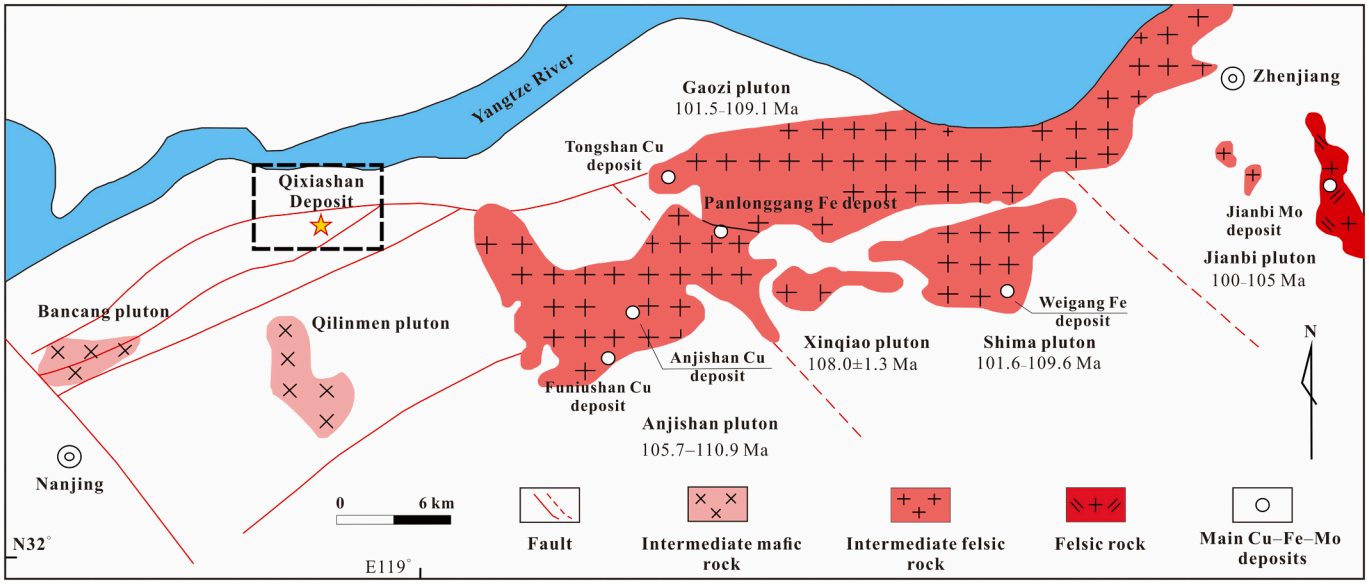

Fig. 2. Simplified geological map of the intrusive bodies in the Nanjing–Zhenjiang region (modified from Zhang et al., 2017). Age data are from Zeng et al., 2013, Wang et al., 2014, Sun et al., 2014, Guan et al., 2015.

3. Deposit geology

The Qixiashan Pb–Zn–Ag deposit covers an area of 25 km^2 and consists mainly of six ore sections: Sanmaogong, Pingshantou, Huzhaoshan, Beixiangshan, Ganjiaxiang, and Xiku (Fig. 3a). The strata in the Qixiashan deposit consist of sandstone and siltstone of the Silurian Fentou Formation (S_{2-3}), quartz sandstone and shale of the upper Devonian Wutong Formation (D_3), sandstone and shale of the lower Carboniferous Gaolishan Formation (C_1), limestone of the upper Carboniferous Chuanshan Formation (C_3), and sandstone and marl of the lower Triassic Xiangshan Formation (J_{1-2}) (Fig. 3a, b). Quaternary strata are dominated by slope wash and alluvium, and gossan and manganese caprocks occur locally at the surface. The limestones of the middle Carboniferous Huanglong formation (C_2) and the lower Permian Qixia Formation (P_1) are the main host strata of Qixiashan Pb—Zn orebodies (Zhang et al., 2017). However, they are not exposed at the surface, and are underlain by sandstone of the lower Carboniferous Gaolishan Formation (Sun et al., 2020).

The strata in the mining area can be divided into upper and lower structural layers, separated by a high-angle unconformity (Fig. 3c). The lower structural layer consists of the Qixiashan–Ganjiaxiang anticlinorium, whose strata include Silurian–Triassic marine, continental, and marine–continental carbonates and clastic rocks. The upper structural layer consists of an anticline composed of Jurassic continental clastic and pyroclastic rocks. Fault structures, formed mainly by the Indosinian and Yanshanian orogenies, are the main ore-hosting structures, including the ENE-trending F_2 and F_3 faults that cut the Gaolishan and Huanglong Formations (Fig. 3). A small number of faults were formed after Pb-Zn mineralization (Gui, 2012; Zhang, 2015).

There are >70 orebodies in the Qixiashan deposit. The Huzhaoshan ore section accounts for 90 % of the total Pb—Zn reserves of this deposit (Gui, 2012; Zhang, 2015). A total of 21 orebodies, mainly on lines 2 to 46, run parallel to the bedding of the host rocks. Most of the orebodies are controlled by an ENE-striking fault and have pinch and swell structures along both the strike and dip directions (Sun et al., 2020). The Pb—Zn orebodies are distributed along the central axis of the main orebody, surrounded by sulfide orebodies (i.e., pyrite-rich; Fig. 3c). Wall-rock alteration is relatively weak in this deposit, comprising light-colored alteration zones at the top and base of the orebody that are tens of centimeters wide (Zhang et al., 2017). Silicification, carbonatization, marbleization, chloritization, and sericitization are visible in the limestone host rocks. Sporadic tremolite, diopside, epidote, chlorite, and other alteration minerals have been found in the deeper fracture zones of the main orebody (e.g., in the Ganjiaxiang ore section), where the proportion of copper minerals is much higher in other sections (Guo et al., 1985; Chen, 1992; Xu and Zeng, 2006; Gui, 2012; Sun et al., 2019).

The main ore minerals in the Qixiashan deposit include pyrite, galena, sphalerite, rhodochrosite, magnetite, arsenopyrite and argentiferous minerals. The dominant silver minerals are argentite (Ag_2S) and electrum (Zhang et al., 2017; Sun et al., 2020). The main gangue minerals are quartz, calcite, dolomite and sericite. The ore structures are mainly massive, disseminated, and brecciated, with banded deposits and veinlets (Fig. 4). The ores show replacement and corrosion, and are granular subhedral–anhedral and micro-cataclastic (Fig. 5).

Based on detailed optical and SEM petrographic observations, along with cross-cutting relationships between hydrothermal veins and mineral assemblages, four hydrothermal stages were identified: (1) the pre-ore pyrite stage (stage I), (2) the Pb–Zn–pyrite stage (stage II), (3) the Pb–Zn–Ag stage (stage III), and (4) the carbonate stage (stage IV). Stage I is represented by euhedral–subhedral, medium-grained (50–500 μm) pyrite (Py-1). The disseminated Py-1 is found in sulfide orebodies and the host limestone (Fig. 4b), and is generally nonporous and almost free of mineral inclusions. Py-1 generally shows structural overprinting, which is indicated by cataclastic textures and replacement or corrosion by subsequent hydrothermal phases (e.g., sphalerite and galena; Fig. 5c). Stage-II sulfide minerals (sphalerite, galena, pyrite, and minor chalcopyrite) occur mainly as veins that cut and replace the host rock and previous sulfides phases (Figs. 4c, 5c). Microscope observations show that stage II sphalerite (Sph-1) is mostly opaque (Fig. 5a) or oscillatory zoned, and is affected by 'chalcopyrite disease' (Fig. 5d). Sph-1 is found mainly in the deeper zones of the Pb—Zn orebodies. Porous pyrite that formed during stage II (Py-2) occurs as anhedral to subhedral, fine- to medium-grained crystals (<50–500 μm). The porosity of most Py-2 is 1–10 %. Most of pores (> 60 %) contain microscopic mineral inclusions (e.g., galena, arsenopyrite; Fig. 5h). Py-2 is closely associated with galena and sphalerite precipitation (Fig. 5e). Magnetite crystallization also occurred during the early part of this stage, and subhedral magnetite is surrounded by galena and sphalerite (Fig. 5d, g). The intensity of Pb—Zn mineralization decreased gradually during stage III. Translucent sphalerite (Sph-2) was formed during this stage (Fig. 5a, b), in shallower zones than Sph-1. The formation of clear, euhedral–subhedral pyrite (Py-3) was coeval with quartz (Fig. 5f). Py-3

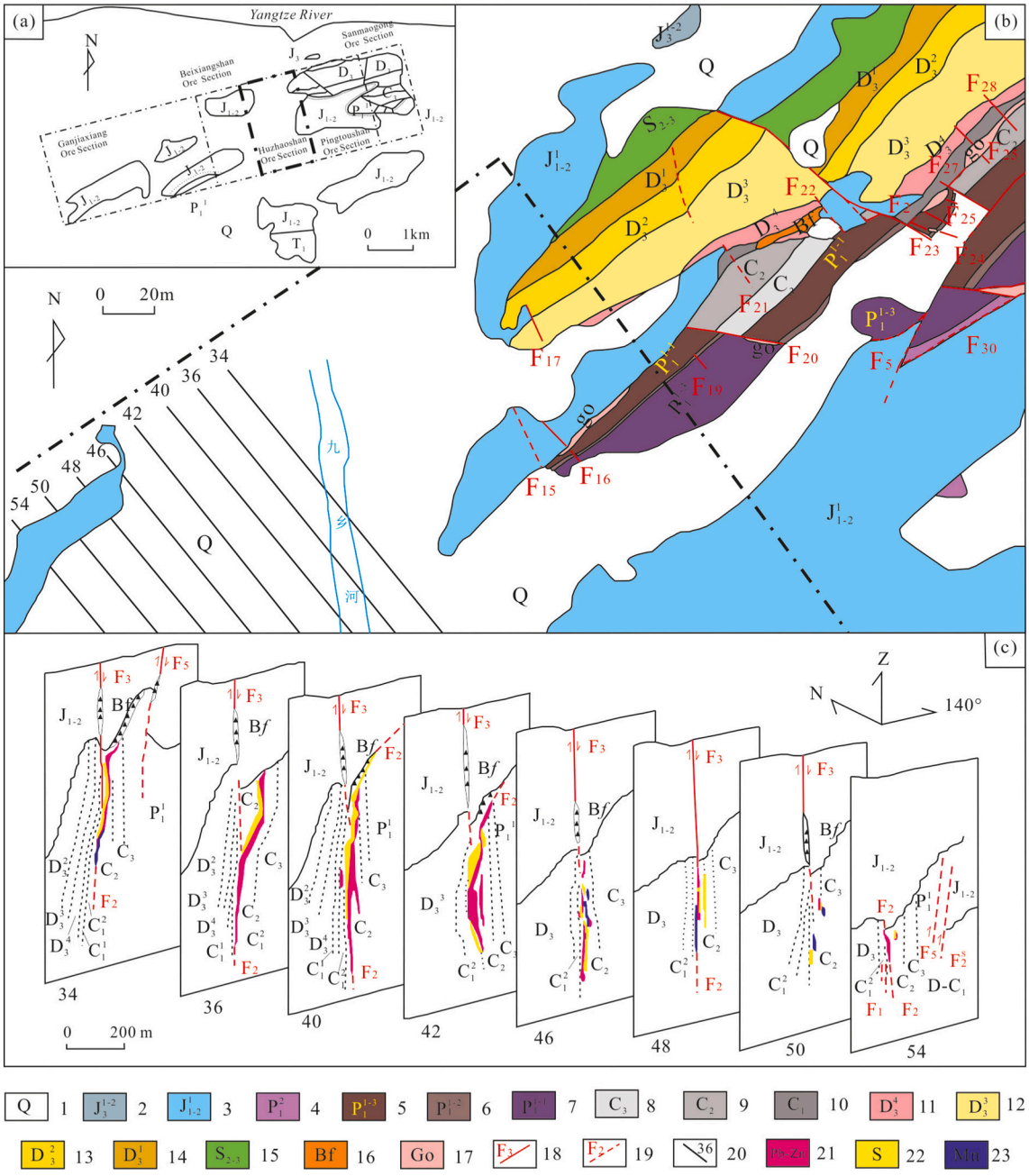

Fig. 3. (a) Overview of the Qixiashan deposit. (b) Geological map and (c) cross-section of the Huzhaoshan ore section (modified from Zhang et al., 2017).
1: Quaternary, 2: Jurassic volcanic rocks, 3: lowest member of the Nanxiangshan Fm., 4: Gufeng Fm., 5, 6, 7: third lowest to the lowest members of the Qixia Fm., respectively, 8: Chuanshan Fm., 9: Huanglong Fm., 10: Gaolishan Fm., 11–14: fourth lowest to lowest members of the Wutong Fm., respectively, 15: Fentou Group, 16: structural breccia and fracture zone, 17: Fe and Mn cap, 18: overserved faults and fault numbers, 19: inferred faults and fault numbers, 20: prospecting lines and numbers, 21: Pb—Zn orebody, 22: sulfide orebody, 23: Mn orebody.

surrounds Py-2 and is zoned (Fig. 5i). In addition, the precipitated rhodochrosite (Fig. 4f) and argentiferous minerals (e.g., electrum) occur along cleavage planes (Fig. 5i). Finally, calcite and quartz veins that cut the early mineralization formed during the carbonate stage (stage IV; Fig. 4f). The detailed paragenetic sequence of the major minerals is shown in Fig. 6.

4. Sampling and analytical methods

Samples were collected from underground mines, mainly from the KK4603 and KK4201 boreholes in the Huzhaoshan ore section. Polished thin sections were then prepared and examined under reflected and transmitted light. After detailed petrographic investigation, six representative samples (pyrite and sphalerite) from different paragenetic stages and depths were selected to cover the temporal evolution of the mineralization. In situ LA–ICP–MS minor and trace elements analyses were performed on pyrite grains from four samples and sphalerite grains from three samples. As well as spot analyses, an oscillatory-zoned sphalerite was selected for LA–ICP–MS element mapping to characterize the relationships between minor and trace elements. There are no obvious inclusions in the areas of the sulfides selected for analysis.

Back-scatter electron (BSE) imaging was conducted to identify zoning as well as the different generations of pyrite using a JEOL JSM-7800F SEM at the State Key Laboratory of Ore Deposit Geochemistry

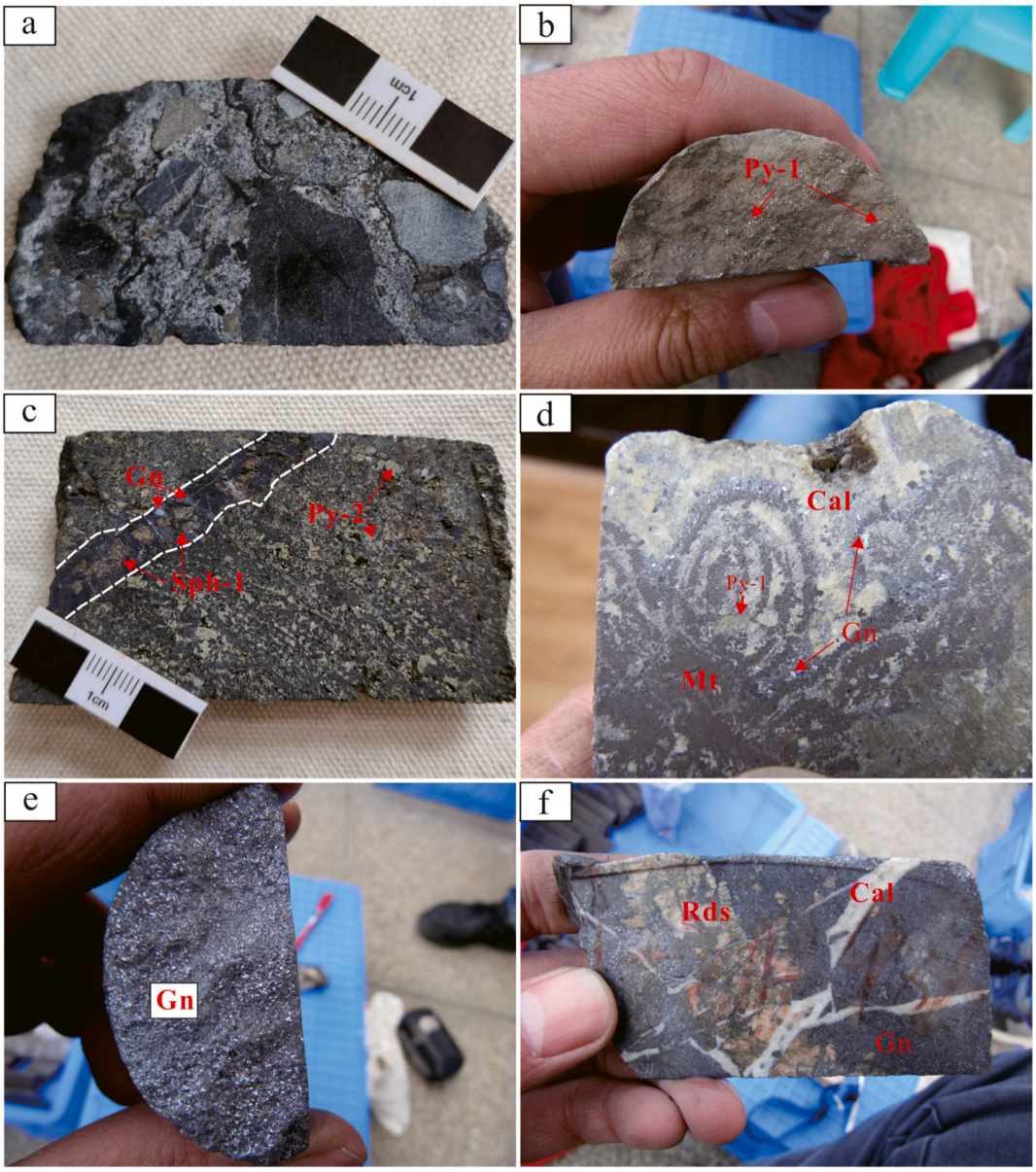

Fig. 4. Representative samples from the Qixiashan deposit. (a) Sandstone breccia. (b) Disseminated pre-ore pyrite (Py-1) in limestone. (c) Subhedral stage-II pyrite, galena, and sphalerite. (d) Pyrite (Py-1) surrounded by intensely folded magnetite with minor galena. (e) High-grade massive galena. (f) Massive galena cut by a later rhodochrosite vein, both of which are cut by a later calcite vein. Py: pyrite, Sph: sphalerite, Gn: galena, Mt.: magnetite, Rds: rhodochrosite, Q: quartz, Cal: Calcite.

(SKLODG), Institute of Geochemistry, Chinese Academy of Science (IGCAS), Guiyang, China, with an accelerating voltage of 20 kV and a beam current of 10 nA.

LA–ICP–MS analysis was carried out using an Agilent 7700× quadrupole ICP–MS coupled with a COMPex-Pro 193 nm coherent ArF excimer laser at the SKLODG. Grains from each sample were selected under the SEM to avoid compositional heterogeneities and inclusions at the grain surface. The ablated aerosol was mixed with Ar (900 ml/min) as the transport gas before exiting the cell. Each analysis consisted of ~30 s of background acquisition (gas blank), followed by 60 s of data collection. Ablation was performed using a spot diameter of 26 μm, a pulse frequency of 5 Hz, and fluence of 3 J cm^{-2}. The Peru Py reference standard was used to calibrate the S and Fe contents. GSE-1G and GSD-1G were used to calibrate lithophile element contents, and STDGL-3 was used to calibrate chalcophile and siderophile element contents (Danyushevsky et al., 2011). The preferred composition of the USGS reference glasses are from the GeoReM database (http://georem.mpch-mainz.gwgd.de/). The MASS-1 sulfide reference standard was analyzed as an unknown sample to check the accuracy of the analyses. STDGL3 was measured at the beginning and end of every 10 sample analyses, along with two analyses of GSE-1G and GSD-1G and one analysis of MASS-1. twenty-two elements were chosen for spot analysis (S, Ti, Mn, Fe, Co, Ni, Cu, Zn, Ga, As, Se, Mo, Ag, Cd, In, Sn, Sb, Te, Au, Tl, Pb, Bi).

LA–ICP–MS mapping of an oscillatory-zoned sphalerite (Sph-1) was also conducted using the instruments described above. An area of 0.5 × 0.5 mm was selected based on detailed petrographic observations and then ablated over a series of parallel lines using a beam diameter of 7 μm, a scan speed of 7 μm/s, and a shot frequency of 10 Hz. The same 22 elements chosen for spot analyses were also chosen for mapping. The acquisition time was 0.006 s for most elements and 0.009 s for ^{107}Ag and ^{197}Au. The total sweep time was ~0.3 s. Two line ablations of STDGL3, GSE-1G, and GSD-1G were carried out before and after the mapping, and were used to calibrate the trace element contents and to monitor analytical drift, which was shown to be negligible.

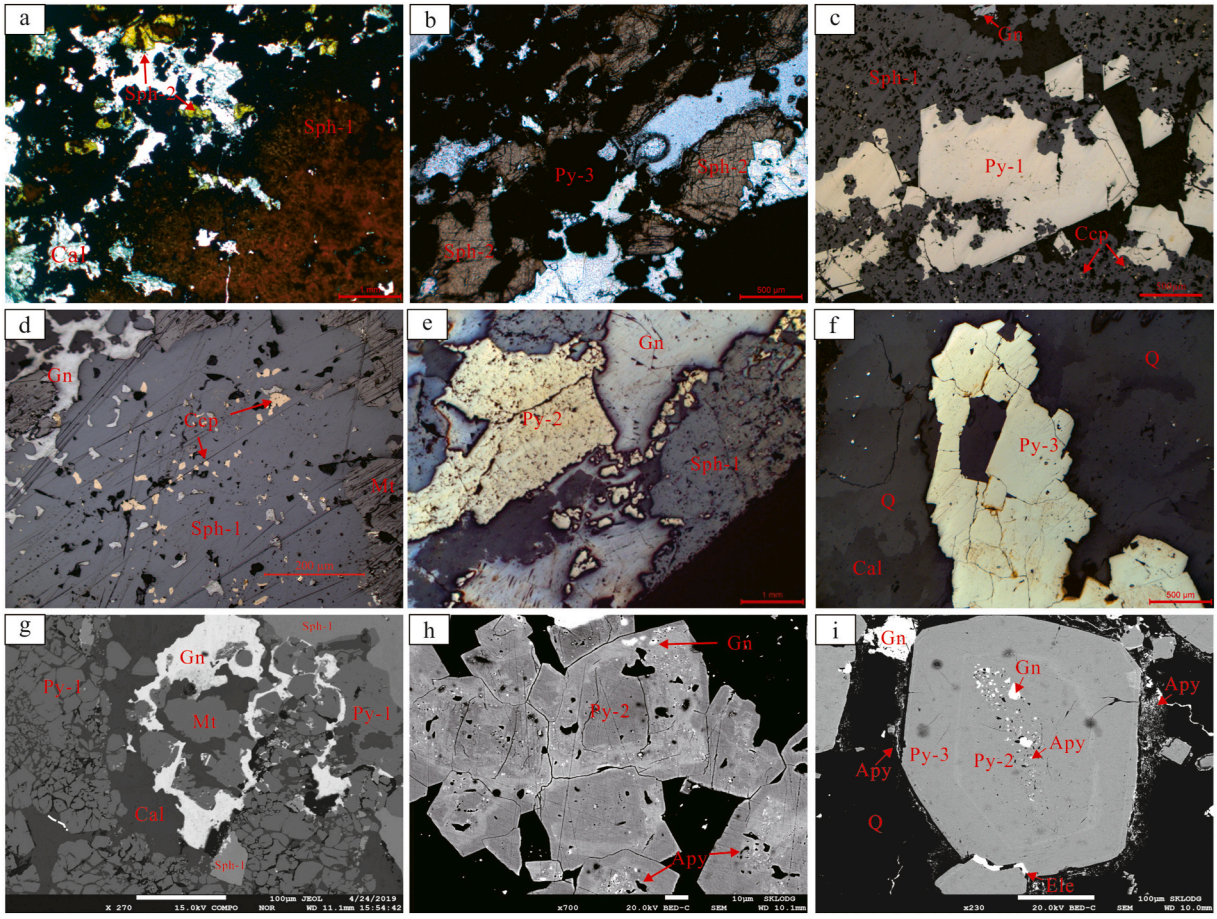

Fig. 5. Microphotographs of ore samples from the Qixiashan deposit (a, b: cross-polarized light, c-f: reflected light, g-i: BSE). (a) Opaque sphalerite (Sph-1) is surrounded by translucent sphalerite (Sph-2). (b) Translucent Sph-2 coexisting with euhedral–subhedral pyrite (Py-3). (c) Euhedral–subhedral pyrite (Py-1) is surrounded and corroded by subsequent sphalerite (Sph-1) and galena grains. (d) Anhedral galena and magnetite, and subhedral sphalerite with 'chalcopyrite disease'. (e) Porous pyrite (Py-2) coexists with subhedral sphalerite (Sph-1) and galena grains. (f) Euhedral-subhedral quartz and pyrite (Py-3) of stage III. (g) Subhedral pre-ore pyrite (Py-1) and magnetite replaced and surrounded by sphalerite (Sph-1) and galena, respectively. (h) Porous pyrite (Py-2) with oscillatory zoning and minor arsenopyrite and galena inclusions. (i) Py-3 bordering porous pyrite (contacts marked with white lines), with minor electrum in microfractures and interstitial spaces. Py: pyrite, Sph: sphalerite, Gn: galena, Apy: arsenopyrite, Mt.: magnetite, Elc: electrum, Rds: rhodochrosite, Q: quartz, Cal: Calcite.

5. Analytical results

5.1. LA–ICP–MS sulfide depth profiling

Minor and trace elements in sulfides may occur in several forms: as solid solution within the crystal lattice, invisible nanoparticles, or visible micron-sized inclusions of sulfide, silicate, or oxide minerals (Huston et al., 1995; Cook et al., 2009; Thomas et al., 2011; Ciobanu et al., 2012). Targets for spots were selected after excluding regions with visible inclusions, to ensure that minor and trace elements in solid solution or nanoparticles were analyzed. However, lattice-hosted elements and those in nanometer- and micron-scale inclusions are unavoidable, even at the scale of the electron beam (Cook et al., 2009). Nevertheless, time-resolved LA–ICP–MS depth profiles are useful for understanding the distribution of minor and trace elements. Representative time-resolved LA–ICP–MS depth profiles for each generation of pyrite and sphalerite are shown in Figs. 7 and 8.

In pyrite, the ablation profiles of some elements (e.g., Co, Ni, As, Se, Ag) are smooth and consistent with major element profiles (Fe and S; Fig. 7a), indicating that these elements are homogenously distributed at the scale of beam. Other elements, including Pb, Zn, and Mn, yield elevated and spiky profiles (Fig. 7c), suggesting that these elements exist mainly in inclusions (e.g., galena and sphalerite) within pyrite. The content of most elements is much lower in Py-3 than in the other generations of pyrite (Fig. 7d), and cannot be used for assessing the distribution of minor and trace elements.

Depth profiles in sphalerite (Fig. 8a) show that Fe, Mn, and Cd yield smooth patterns similar to that of Zn, suggesting that they are homogenously distributed at the scale of the beam. Other elements, including Pb, Cu, Sb, Ag, yeild irregular and spiky profiles, suggesting that those elements exist mainly in inclusions (e.g., chalcopyrite and galena) within sphalerite. Minor and trace element contents are much lower in Sph-2 than in Sph-1, and cannot be used to assess the distribution of those elements.

5.2. Pyrite compositions

A total of 21 individual LA–ICP–MS spot analyses were conducted on pyrite grains. Because the presence of inclusions is suggested by the compositional variation in the depth profiles, we selected the more homogenous profiles as a better record of the lattice-bound trace element contents of the pyrite. The results of in situ minor and trace element analyses are listed in Table 1. Minor and trace element compositions of Py-1, Py-2, and Py-3 are shown in Fig. 9.

The minor and trace element contents of the pyrite are clearly correlated with the mineralization sequence. Py-1 yields higher Co (6.27–127 ppm; mean = 80.4 ppm) and Ni (11.9–785 ppm; mean = 326 ppm) contents than Py-2 and Py-3. Other elements with elevated

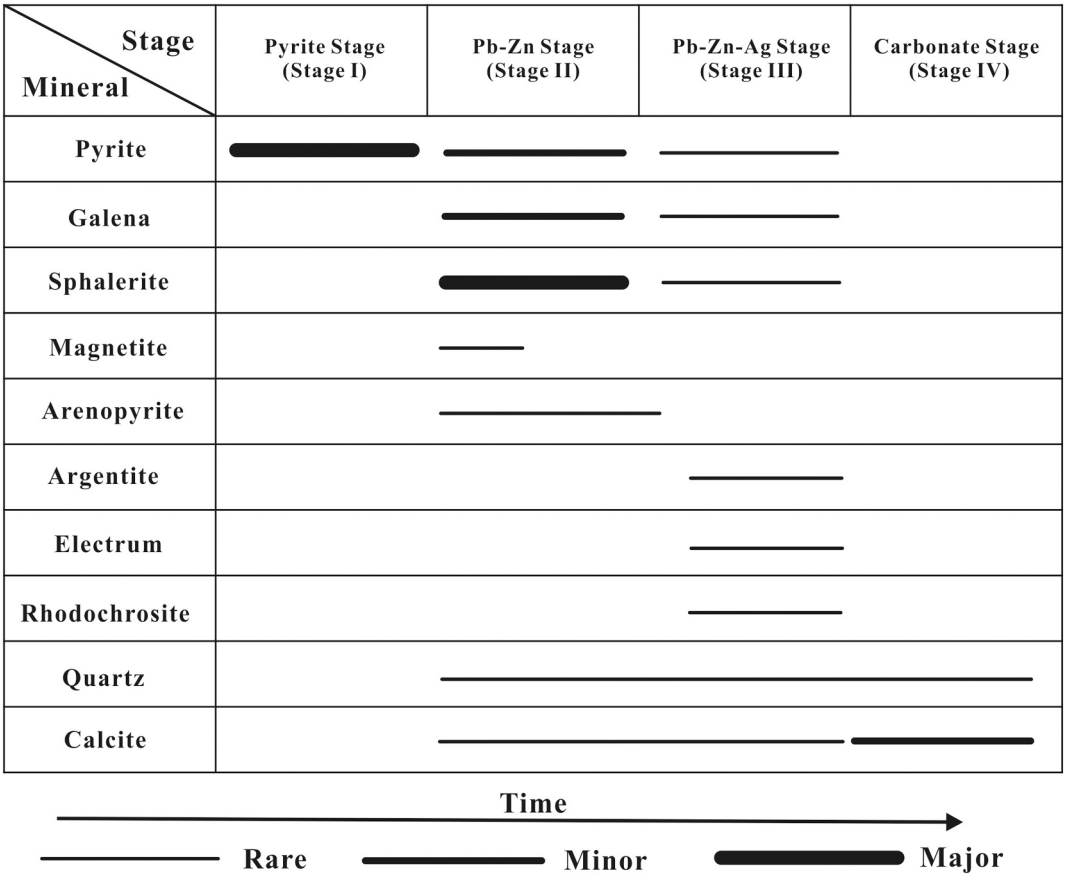

Fig. 6. Paragenetic sequences of major minerals in the Qixiashan deposit.

contents in Py-1 include Cu (31.0–68.2 ppm; mean = 48.9 ppm) and As (2777–8903 ppm; mean = 4920 ppm). Py-2 has lower Co (0.06–0.19 ppm; mean = 0.11 ppm), Ni (0.19–0.70 ppm; mean = 0.35 ppm), and As (797–6649 ppm; mean = 2393 ppm) contents than Py-1. However, it has anomalous Mn (42.5–970 ppm; mean = 469 ppm), Zn (2.22–35.2 ppm; mean = 12.1 ppm), Se (5.24–11.31 ppm, mean = 7.57 ppm), and Pb (490–2158 ppm; mean = 850 ppm) contents. The minor and trace element contents in Py-3 are generally low, and some are below detection limits. The results of the spot analyses of Py-1, Py-2 and Py-3 are consistent with the time-resolved LA–ICP–MS depth profiles.

5.3. Compositions and element distribution in sphalerite

A total of 22 individual LA–ICP–MS spot analyses and element maps were completed on sphalerite grains. The results of in situ minor and trace element analyses are listed in Table 2. Overall, sphalerite from the Qixiashan deposit is characterized by enrichment in Fe, Mn, In, and Sn, and depletion in Co, Ni, Ge, Ga, and Cd. Like the pyrite, the minor and trace element contents in sphalerite vary with paragenetic stage. Opaque or oscillatory-zoned Sph-1 yields higher Fe (4.20–10.9 wt%, mean = 8.70 wt%), Mn (0.003–1.29 wt%, mean = 0.05 wt%), Cu (15.1–2993 ppm, mean = 583 ppm), Ag (1.09–311 ppm, mean = 63.4 ppm), In (1.58–153 ppm, mean = 44.2 pm), Sn (0.11–745 ppm, mean = 79.4 ppm), and Pb (0.27–1674 ppm, mean = 210 ppm) contents. In contrast, the translucent sphalerite yields substantially lower Fe (1837–2360 ppm, mean = 2038 ppm), Mn (19.3–23.4 ppm, mean = 21.2 ppm), Cu (39.8–50.9 ppm, mean 44.2 ppm), Ag (2.13–21.4 ppm, mean = 8.82 ppm), In (0.02–0.05 ppm, mean = 0.03 pm), Sn (5.94–13.4 ppm, mean = 8.95 ppm) and Pb (1.03–6.76 ppm, mean = 2.97 ppm) contents. The Cd (2904–5004 ppm, mean = 3802 ppm) and Ge (0.91–7.18 ppm, mean = 1.70 ppm) contents of the sphalerite do not vary significantly between Sph-1 and Sph-2. The Ga content (1.30–583 ppm, mean = 72.0 ppm) of the sphalerite grains is not uniform, even within a single sample. The As, Co, and Ni contents is low with some analyses below detection limits.

LA–ICP–MS element mapping of an oscillatory-zoned Sph-1 revealed distinct patterns in the distribution of Fe, Mn, Sn, Sb, Pb, Cu, In, and Ag. Notably, Fe, Cu, and In show oscillatory zoning from core to rim, unlike Mn. Lead is irregularly distributed, indicating that it may exist in mineral inclusions in the sphalerite. Silver, Sb, and Sn have similar distributions and are enriched in the core and small fractures, which is consistent with the appearance of argentiferous minerals (e.g. electrum) during the subsequent Pb—Zn mineralization stage (stage III).

6. Discussion

6.1. Genesis of the Qixiashan deposit

The genesis of the Qixiashan deposit has long been debated, with proposed models including SEDEX (e.g., Gui, 2012)), magmatic hydrothermal (e.g., Zhang, 2015; Zhang et al., 2017; Gong et al., 2020), and a sedimentary deposit with subsequent hydrothermal overprinting (e.g., Sun et al., 2018, 2020).

The abundances and distribution of minor and trace elements in sphalerite have been used to constrain the genesis of deposits worldwide as trace element compositions can provide genetic information (Zhang, 1987; Di Benedetto et al., 2005; Gottesmann and Kampe, 2007; Cook et al., 2009; Wang et al., 2010; Ye et al., 2011, 2012, 2016). In general, Mississippi valley-type (MVT) Pb—Zn deposits are enriched in Cd, Ge, and Ga, and depleted in Fe, Mn, In, Sn, and Co (e.g., the Niujiaotang, Mengxing, and Huize Pb—Zn deposits, China; Ye et al., 2011). Volcanogenic massive sulfides (VMS) deposits are enriched in Mn and Co, and depleted in In (e.g., Marketorp, Sweden and Sauda, Norway; Cook et al.,

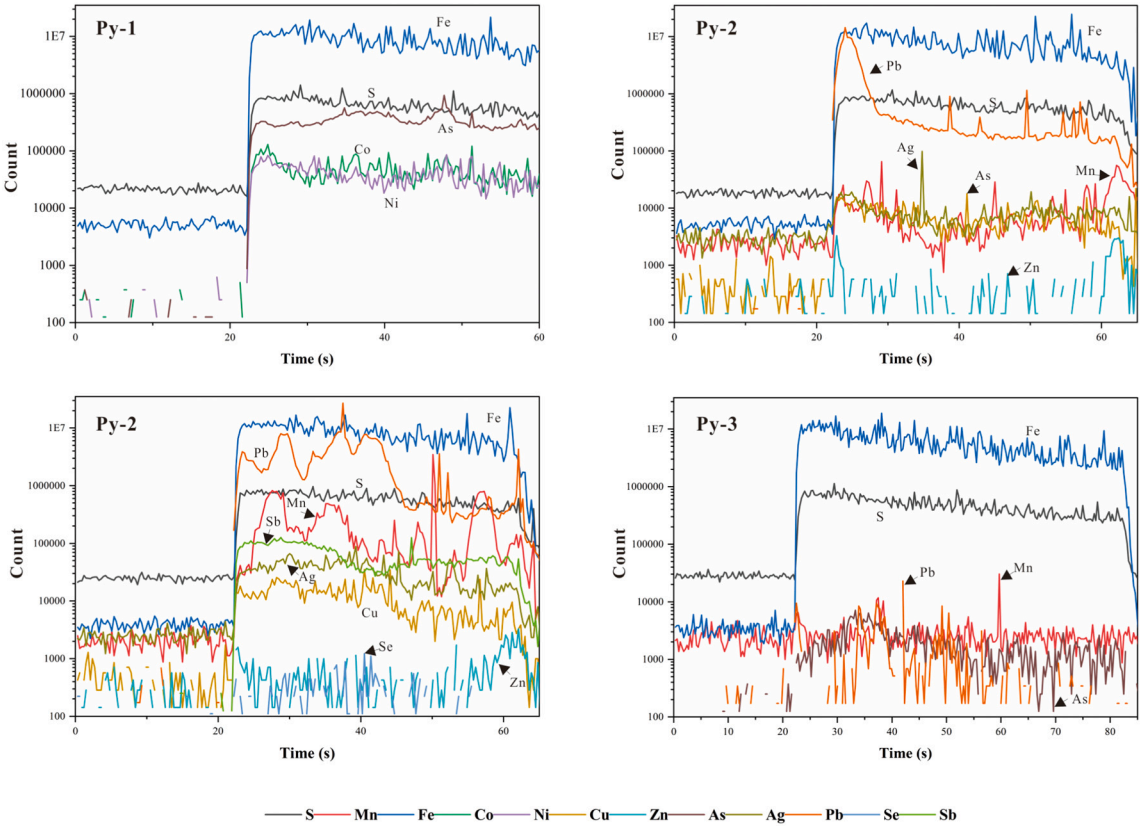

Fig. 7. Representative time-resolved LA–ICP–MS depth profiles of pyrite from the Qixiashan deposit.

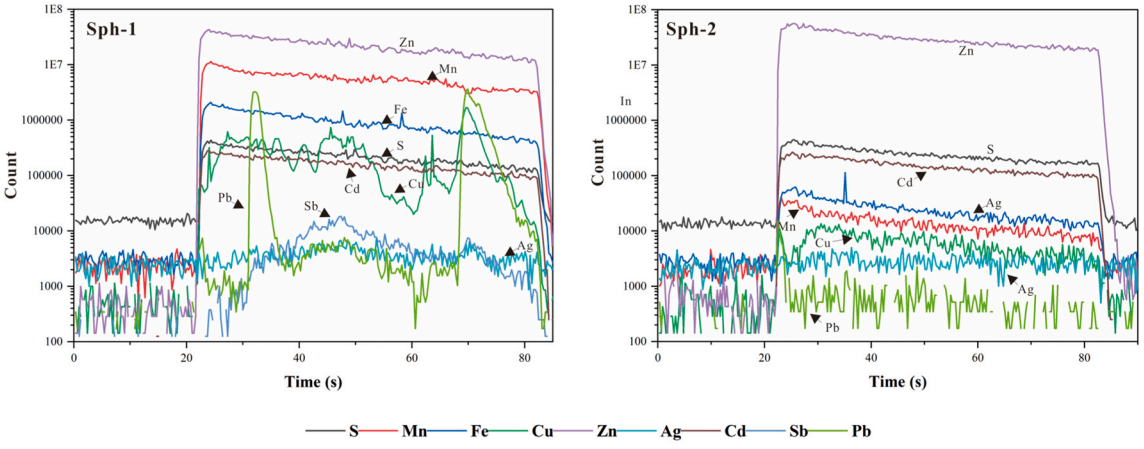

Fig. 8. Representative time-resolved LA–ICP–MS depth profiles of sphalerite from the Qixiashan deposit.

2009). Skarn-type deposits are characterized by elevated Mn and Co contents, and the distal parts of those deposits have low Sn contents (e.g., Hetaoping and Luziyuan Pb—Zn deposits, China; Ye et al., 2012). Epithermal deposits are characterized by enrichment in Fe, Mn, In and Sn, and depletion in Cd, Ga, and Ge (e.g., Baia de Aries and Hanes, Romania; Cook et al., 2009).

The minor and trace element compositions of sphalerite from the Qixiashan deposit are characterized by enrichment in Fe, Mn, In, and Sn, and depletion in Cd and Ge (Table 1). The Fe and Mn contents are much higher than those of MVT Pb—Zn deposits (e.g., Mn = 96.3 ppm and Fe = 2.12 wt% in the Huize deposit), and the In content is higher than that in VMS deposits. Almost all In-rich sphalerite grains in Pb—Zn deposits are related to magmatic activity (Zhang et al., 2003; Cook et al., 2009). In-rich Pb—Zn deposits are also rich in Sn (e.g. the Dulong Pb—Zn, Toyoha, and Potosi deposits), which is related to the co-migration of In and Sn in magmatic hydrothermal fluids (Zhang et al., 2003; Zhu et al., 2006; Shimizu and Morishita, 2012). However, the Co contents of sphalerite grains from the Qixiashan deposit are mostly below the detection limit, unlike those in skarn-type deposits (most >200 ppm; Cook et al., 2009; Ye et al., 2011). On In versus Ge and In versus Co diagrams (Fig. 10), most analyses from the Qixiashan deposit plot close to those from other epithermal deposits. Thus, we propose that the Qixiashan deposit is closely related to magmatic activity. Furthermore, previous studies have shown that the sulfide minerals from different stages record $\delta^{34}S_{V\text{-}CDT}$ values of −4.44 ‰ and + 7.22 ‰, consistent with a magmatic sulfur source (Zhang et al., 2017, 2019; Gong et al., 2020).

Table 1
The LA-ICP-MS spot analyses of different generations of pyrite from the Qixiashan deposit.

Stage of mineralization	Sample	Mn	Co	Ni	Cu	Zn	As	Se	Ag	Sb	Pb
	(ppm)										
Py 1	51-py-1	39.9	6.27	11.9	57.6	13.0	8903	4.30	180	22.5	274
	78-Py-1	49.0	55.7	215	31.0	27.3	3140	<DL	12.2	53.9	401
	78-Py-3	84.6	116	595	36.6	2.35	4535	4.38	25.4	40.2	420
	78-Py-6	54.8	85.4	243	36.7	2.4	2777	<DL	13.4	82.3	878
	78-Py-8	7.73	65.3	179	54.2	2.2	2933	<DL	18.7	101	564
	78-Py-9	8.82	127	259	57.8	<DL	4589	<DL	25.3	128	668
	78-Py-13	2.71	107	785	68.2	6.57	7561	<DL	3.88	12.2	216
Py 2	16-py-2	42.5	<DL	0.44	18.2	33.0	2471	5.24	49.5	57.3	629
	16-py-3	172	<DL	<DL	13.7	35.2	797	5.48	35.5	100	490
	16-py-4	600	0.06	0.30	8.05	2.36	895	<DL	34.7	63.8	1093
	16-py-11	167	0.19	1.36	49.7	4.68	6461	11.31	54.99	54.1	132
	16-py-20	550	0.07	<DL	15.1	4.15	1109	6.72	19.9	134	513
	16-py-21	970	<DL	0.70	28.2	2.22	6649	8.36	45.1	63.9	935
	16-py-37	781	<DL	<DL	19.3	2.92	2806	8.31	51.2	74.5	2158
Py 3	38-Py - 1	0.37	0.07	0.96	0.86	<DL	0.76	<DL	<DL	0.15	0.48
	38-Py - 2	<DL	<DL	0.76	0.81	<DL	1.34	<DL	<DL	0.20	1.31
	38-Py - 3	2.51	<DL	3.82	15.6	1.96	221	<DL	3.90	0.78	22.3
	38-Py - 5	1.81	<DL	1.94	7.23	2.02	<DL	<DL	2.09	0.78	33.2
	38-Py - 6	1.01	<DL	2.35	6.95	<DL	292	<DL	2.27	1.60	31.3
	38-Py - 8	<DL	<DL	4.16	<DL	1.18	<DL	<DL	<DL	0.23	3.21
	38-Py - 15	2.00	<DL	1.95	3.03	<DL	<DL	<DL	1.85	<DL	6.19
Detection limit (DL)		0.32	0.04	0.2	0.6	1.07	0.5	3.25	0.67	0.11	0.11

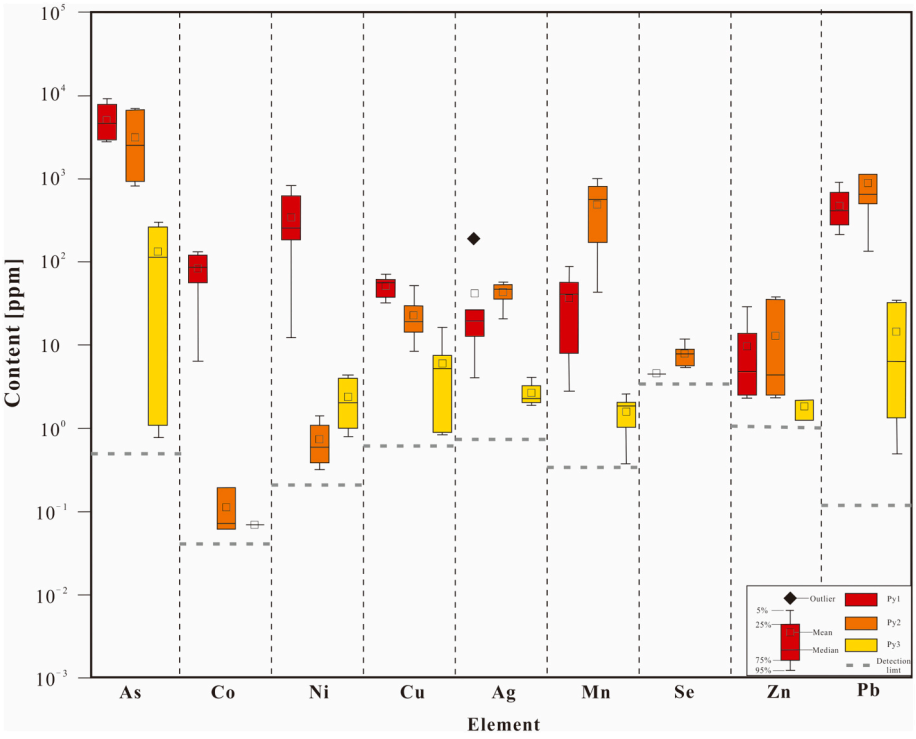

Fig. 9. Minor and trace element contents of the three types of pyrite from the Qixiashan deposit measured by LA–ICP–MS.

Co/Ni ratios can be used to constrain the type of pyrite (Bralia et al., 1979; Bajwah et al., 1987; Large et al., 2009; Reich et al., 2013). Hydrothermal pyrite generally has Co/Ni ratios of >1 (Bralia et al., 1979; Cook, 1996). However, the Co/Ni ratio alone cannot be used to discriminate between deposition environments, because the mobilization of hydrothermal fluid can reduce Co contents, and consequently the Co/Ni ratio (Bralia et al., 1979; Bajwah et al., 1987; Qi et al., 2022). Moreover, felsic rocks, such as granites, usually contain very low Ni content (Zhao et al., 2011; Yuan et al., 2018; Qi et al., 2022). Pyrite grains in the Qixiashan deposit have low Co and Ni contents, which we infer to be linked to long-distance transport and differentiation of intermediate–felsic magma in mining areas.

Previous studies have shown that large-scale magmatism developed during the Yanshanian due to the northwestward subduction of the paleo-Pacific Plate beneath the South China Block (Zhou et al., 2016; Zhang et al., 2017). Many Cu, Fe, Mo, Pb, and Zn deposits related to the contemporaneous magmatic hydrothermal activity formed in the Nanjing-Zhenjiang region, including the Anjishan Cu, Funiushan Cu, and Weigang Fe deposits (Fig. 2; Zhang, 2015). Although the metallogenic age is still uncertain, we propose that the Qixiashan Pb–Zn–Ag deposit is a contemporaneous epithermal deposit in the Yanshanian, and is related to and possibly a distal part of a deep magmatic hydrothermal

Table 2
The LA-ICP-MS Sphot analyses of different generations of sphhalerite from the Qixiashan deposit.

Stage of mineralization	Sample	Mn	Fe	Co	Ni	Cu	Ga	Ge	As	Ag	Cd	In	Sn	Sb	Pb
		(ppm)													
Sph1	38-Sph-1	8856	101,069	< DL	0.21	19.0	1.94	1.61	< DL	1.64	4179	1.58	2.59	< DL	0.27
	38-Sph-3	7341	94,509	0.15	< DL	22.0	1.47	1.33	< DL	2.70	3753	4.64	3.37	0.62	3.79
	38-Sph-4	6246	95,906	0.08	0.02	15.1	< DL	1.18	< DL	1.09	3568	6.66	< DL	< DL	2.05
	38-Sph-5	6890	93,779	< DL	< DL	135	< DL	2.24	< DL	5.20	3605	7.46	0.33	0.46	9.13
	38-Sph-6	4472	88,347	0.02	0.07	114	1.83	1.31	3.77	4.78	3433	7.70	1.34	7.06	2.73
	38-Sph-7	12,888	106,540	0	< DL	2994	4.06	1.48	8.67	8.90	4169	2.62	3.59	35.3	1325
	38-Sph-8	11,436	90,161	< DL	< DL	315	17.0	1.55	15.42	8.58	3790	2.93	2.82	21.8	9.11
	38-Sph-9	12,496	102,926	< DL	< DL	197	2.16	1.47	1.19	7.40	3931	2.93	0.90	13.0	5.25
	71-Sph - 1	534	109,379	< DL	< DL	301	149	1.90	< DL	68.4	5004	30.5	74.0	6.11	88.5
	71-Sph - 2	367	97,874	0.03	0.42	1145	150	1.87	6.63	312	4390	31.5	209	47.0	120
	71-Sph - 3	302	100,897	0.04	0.25	1653	584	7.18	18.4	305	4844	154	746	90.0	42.3
	71-Sph - 4	782	86,909	< DL	0.05	1590	131	1.53	2.25	200	4774	24.7	122	9.11	42.6
	71-Sph - 5	2129	75,058	0.04	< DL	660	68.6	1.45	9.05	85.6	3311	44.6	104	5.82	1675
	71-Sph - 6	1164	81,985	0.06	0.30	163	2.42	1.09	< DL	26.4	3768	154	0.11	0.52	70.4
	71-Sph - 7	1245	42,035	0.06	< DL	122	79.6	0.99	< DL	11.6	3044	78.4	0.72	< DL	91.6
	71-Sph - 8	4901	55,646	< DL	0.14	73.6	1.30	1.14	< DL	9.58	3692	110	0.18	< DL	83.3
	71-Sph - 9	1835	57,368	< DL	0.46	97.4	36.7	1.03	< DL	19.0	3862	88.4	0.51	2.02	14.1
Sph2	11-Sph - 1	19.3	1838	0	0.18	42.0	30.8	1.21	0.77	3.00	3008	0.02	5.94	3.65	1.03
	11-Sph - 2	21.0	1920	0.07	< DL	39.8	21.7	0.91	< DL	2.13	2904	0.05	13.4	3.03	1.11
	11-Sph - 3	55.9	1988	0.10	< DL	65.6	25.6	1.30	15.7	15.1	3012	< DL	10.1	31.7	16.6
	11-Sph - 4	25.1	2462	0.08	0.28	27.2	14.2	0.93	1.80	4.74	2904	< DL	3.49	7.39	2.75
	11-Sph - 5	23.4	2360	0	< DL	50.9	21.1	< DL	2.35	21.3	3007	< DL	7.45	32.4	6.76
Detection limit (DL)		0.51	28.1	0.01	0.04	0.96	0.13	0.72	0.66	1.15	0.41	0.02	0.11	0.16	0.42

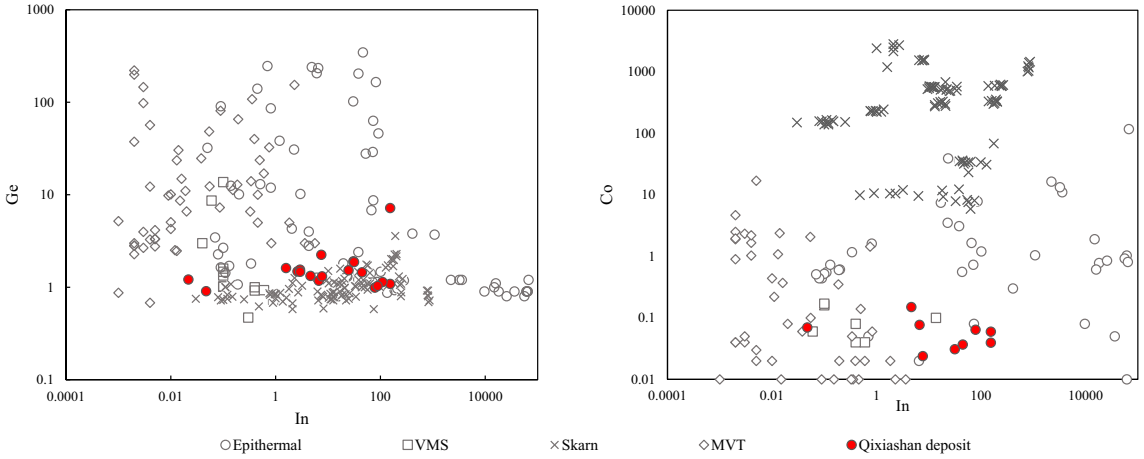

Fig. 10. Ge versus In and Co versus In diagrams for sphalerite from the Qixiashan deposit. Data from skarn and MVT deposits are from Ye et al. (2011), and data of epithermal and VMS deposits are from Cook et al. (2009).

system.

6.2. Evolution of ore-forming fluid

The trace element contents of sulfide minerals can reflect the physicochemical conditions of the hydrothermal fluids from which they were precipitated, including the temperature, pressure, fO_2, and pH (Fernández et al., 2000; Cook et al., 2009; Large et al., 2009; Maslennikov et al., 2009; Ye et al., 2011; Zhang et al., 2017; Feng et al., 2020; Li et al., 2020). LA–ICP–MS and BSE analyses show that minerals formed during different stages in the Qixiashan deposit display different trace element characteristics. A comparative study of the minor and trace element compositions of pyrite and sphalerite can provide valuable information on the evolution of the ore-forming fluid.

High temperatures favor the substitution of Fe by Co and Ni in pyrite (Loftus-Hills and Solomon, 1967; Clark et al., 2004; Migdisov et al., 2011; Grant et al., 2018; Román et al., 2019). A reduction in temperature from 300 to 200 °C can lead to a significant decrease in Co solubility, by up to two orders of magnitude, due to the instability in Co–chloride complexes (Migdisov et al., 2011). In the Qixiashan deposit, the Co content decreases from Py-1 (mean = 80.38 ppm) to Py-2 (mean = 0.03 ppm) and Py-3 (mean = 0.05 ppm; Figs. 9; Table 1), which suggests that the fluid temperature decreased from the pre-ore pyrite stage (stage I) to the later Pb—Zn mineralization stages (stages II and III).

Previous studies have shown that sphalerite which formed at high temperatures is enriched in Fe, Mn, In, and Sn, whereas sphalerite formed at low temperatures is enriched in Cd, Ga, and Ge and is characterized by low In/Ge ratios (Liu et al., 1984; Cai and Zhang, 1996; Ye et al., 2016; Cugerone et al., 2018). Rhodochrosite is widespread in the Qixiashan deposit, indicating that the ore-forming hydrothermal system was rich in Mn. Owing to the surrounding sericitization and chloritization, the Ga contents in the sphalerite differ from those of other epithermal deposits (e.g., mean Ga content = 4.34 ppm in Hanes deposit; Cook et al., 2009). Therefore, Mn and Ga contents cannot be used in this study, and we focus mainly on Fe, In, and Sn to constrain the temperature. The black opaque or oscillatory-zoned Sph-1 yields high Fe (mean = 8.70 %), In (mean = 44.2 ppm), and Sn (mean = 79.4 ppm) contents,

whereas the transparent Sph-2 has substantially lower Fe (mean = 0.21 %), In (mean = 0.03 ppm) and Sn (mean = 8.09 ppm) contents. Thus, it can be inferred that the hydrothermal fluid temperature decreased continuously from the early to late stages, which is consistent with fluid inclusion micro-thermometry (stage I: 280–380 °C; stages II and III: 180–320 °C; stage IV: 80–160 °C; Zhang et al., 2017).

Selenium is a redox-sensitive element, and Se content in pyrite are positively correlated with fO_2 (Large et al., 2017, 2019). In the Qixiashan deposit, the Se content increases from Py-1 (mean = 4.34 ppm) to Py-2 (mean = 7.57 ppm), then decreases at Py-3 (< below the detection level). The low V contents in stage II magnetite also indicate high fO_2 (Nadoll et al., 2014; our unpublished data). Thus, we suggest that stage II was characterized by a relatively high-fO_2 hydrothermal fluid, and the fO_2 of the ore-forming fluids decreased from stage II to stage III.

Sph-2 is often oscillatory zoned, and a LA–ICP–MS element map shows the same core-to-rim variation as spot analyses. Iron, Sn, and Cu contents decrease by an order of magnitude or more from the dark cores to the light rims. Indium and Cd contents decrease to a lesser extent, and Mn contents increases by an order of magnitude or more from cores to rims. Similar oscillatory zoning can be seen in the porous Py-2. In BSE images, Py-2 shows oscillatory zoning, with bright bands yielding elevated As contents (Fig. 5). Zoning in sphalerite and pyrite has been described in many previous studies (e.g., Roedder, 1968; Gagnevin et al., 2014; Velásquez et al., 2014; Wei et al., 2021), which show that changing physicochemical conditions (e.g., pressure, temperature and fO_2) of hydrothermal fluids likely contribute to the formation of oscillatory zoning. In the Huzhaoshan ore section, the EW-trending F_2 is the most important ore-hosting structure. Hence, we speculate that the oscillatory zoning in Sph-1 and Py-2 may be related to pressure fluctuations and repeated local fluid phase separation, when deep-seated, Pb–Zn-rich fluids flowed upward along F_2.

The oscillatory zoning could also reflect an increase in magmatic hydrothermal activity from stage I to II. Previous studies have suggested that slow crystallization of pyrite during hydrothermal processes can drive trace elements out of the pyrite (Large et al., 2007, 2009). Most minor and trace element (e.g., Pb, Zn, As, Ag) contents in the clear euhedral–subhedral Py-3 are substantially lower than those in Py-1 and Py-2, indicating a decrease in magmatic hydrothermal activity from stage II to III. Argentiferous minerals (e.g., electrum) began to precipitate in later small fractures in sulfide minerals (e.g., sphalerite; Fig. 11), suggesting a Ag-rich and Pb-Zn-depleted fluid during stage III.

To summarize, we propose that the temperature of the hydrothermal fluid decreased continuously from the early to late stages. Deep-seated, high-fO_2, Pb—Zn rich fluid migrated along the main fault during stage II, leading to oscillatory zoning in pyrite (Py-2) and sphalerite (Sph-1). The subsequent precipitation of Py-3 suggests a decrease in magmatic hydrothermal activity, and the end of Pb—Zn mineralization.

6.3. Implications for deep exploration

Based on the trace element geochemistry discussed above, we conclud that the Qixiashan deposit is a distal Pb—Zn magmatic hydrothermal deposit related to late Yanshanian magmatic activity. Therefore, corresponding exploration strategies need to be adjusted in light of this result.

Our LA–ICP–MS spot analyses of sphalerite show that the most of black, opaque, or oscillatory-zoned Sph-1, that occur at depth in the Pb—Zn orebodies yield high In, Sn, and Fe contents. In contrast, the transparent Sph-2 at shallow depth yields lower contents of these elements. Previous studies have shown that the substitution of Zn by In, Sn, and Fe in sphalerite is more efficient at higher temperatures (e.g., Cook et al., 2009; Frenzel et al., 2016; Bauer et al., 2019a, 2019b). Sphalerite that formed close to plutons generally has higher In contents than that formed farther from plutons (Huston et al., 1995; Cook et al., 2009; Ye et al., 2011). We suggest that the ore-forming fluid migrated from deep along the main faults in the mining areas affected by the Yanshanian Orogeny. Furthermore, deep exploration boreholes in the Ganjiaxiang ore section revealed significant Cu—Fe mineralization assemblages (e.g., magnetite and chalcopyrite; Gui et al., 2015). Combined with the distribution of peripheral metal deposits, exploration for deep Sn, Cu mineralization has great potential.

In summary, the In, Sn, and Fe contents of sphalerite can be an useful exploration tool to reveal the migration of hydrothermal fluid and for deep prospecting in a distal deposits, especially those with no magmatic

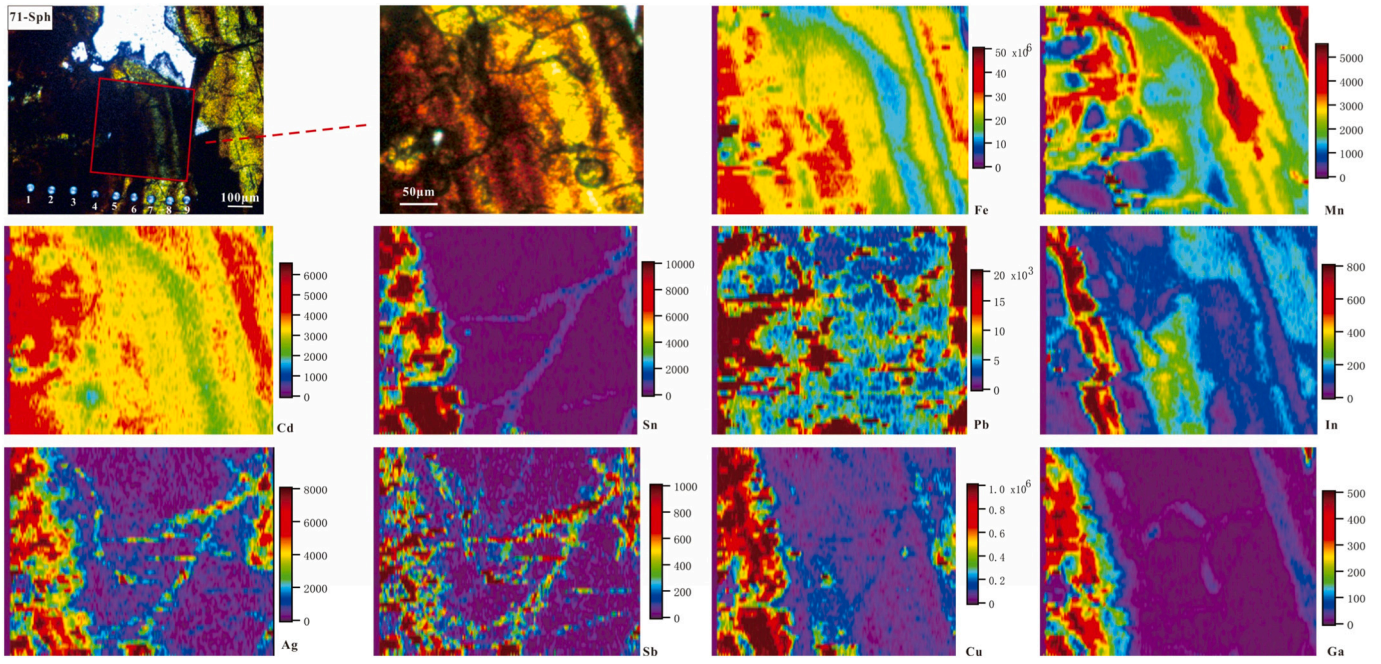

Fig. 11. Elements maps of an oscillatory-zoned sphalerite from the Qixiashan deposit. The red rectangle in the first image indicates the analyzed area, and some sites of spot analyses are also shown. Line ablations were carried out using a 7 μm beam. (For interpretation of the references to colour in this figure legend, the reader is referred to the web version of this article.)

rocks.

7. Conclusions

In situ LA–ICP–MS minor and trace element spot and mapping analyses of sulfide minerals, coupled with detailed microscopic observations, have provided new insights into the genesis and ore-forming processes of the Qixiashan deposit, leading to the following conclusions.

(1) Although no magmatic rocks are observed, sphalerite in the Qixiashan deposit is typically enriched in Fe, Mn, In, and Sn, and depleted in Ge and Cd, indicating Pb—Zn mineralization has magmatic hydrothermal characteristics related to late Yanshanian magmatic activity.
(2) Variations in the minor and trace elements contents (e.g., Co, Ni, and Se in pyrite and Fe, In, and Sn in sphalerite) in the Qixiashan deposit can be ascribed mainly to the evolution of the temperature and fO_2 of the ore-forming fluids from the early to late stages.
(3) Oscillatory zoning in stage-II sphalerite and pyrite reflects pressure fluctuations and repeated local fluid phase separation around the pyrite and sphalerite crystals when deep-seated, Pb–Zn-rich fluid flowed upward along the F_2 fault during stage II. The subsequent precipitation of stage-III pyrite indicates a decrease in magmatic-hydrothermal activity and the end of Pb—Zn mineralization.
(4) In conjunction with the deposit geology, the minor and trace element characteristics of sphalerite from the Qixiashan deposit are indicative of ore-forming fluid conditions and are useful for further deep exploration.

Declaration of competing interest

The authors declare that they have no known competing financial interests or personal relationships that could have appeared to influence the work reported in this paper.

Data availability

Data will be made available on request.

Acknowledgements

This research was supported by the National Natural Science Foundation of China (42273074, 41973049), the Western Young Scholars Project (Class A) of the Chinese Academy of Sciences, and the National Key Research and Development Program of China (2016YFC0600207). We are grateful to Dr. Zhihui Dai, Dr. Shaohua Dong and Ms. Xue Zhang for their support with the analyses.

References

Bajwah, Z.U., Seccombe, P.K., Offler, R., 1987. Trace element distribution, Co:Ni ratios and genesis of the big cadia iron-copper deposit, new south wales, australia. Mineral. Deposita 22 (4), 292–300.
Baker, T., Van Achterberg, E., Ryan, C.G., Lang, J.R., 2004. Composition and evolution of ore fluids in a magmatic-hydrothermal skarn deposit. Geology 32 (2), 117–120.
Bauer, M.E., Burisch, M., Ostendorf, J., Krause, J., Frenzel, M., Seifert, T., Gutzmer, J., 2019a. Trace element geochemistry of sphalerite in contrasting hydrothermal fluid systems of the Freiberg district, Germany: insights from LA-ICP-MS analysis, near-infrared light microthermometry of sphalerite-hosted fluid inclusions, and sulfur isotope geochemistry. Mineral. Deposita 54 (2), 237–262.
Bauer, M.E., Seifert, T., Burisch, M., Krause, J., Richter, N., Gutzmer, J., 2019b. Indium-bearing sulfides from the Hämmerlein skarn deposit, Erzgebirge, Germany: evidence for late-stage diffusion of indium into sphalerite. Mineral. Deposita 54 (2), 175–192.
Bralia, A., Sabatini, G., Troja, F., 1979. A revaluation of the Co/Ni ratio in pyrite as geochemical tool in ore genesis problems. Mineral. Deposita 14 (3), 353–374.
Cai, J.H., Zhang, J.Z., 1996. Typomorphic characteristics of sphalerites in the Yinshan copper , lead and zinc polymetallic deposit, Jiangxi. J. Guilin Univ. Technol. 16 (4), 6 (in Chinese with English abstract).
Chen, F.X., 1992. On the genesis of Dabaoshan Pb-Zn-S deposit, Nanjing. Jiangsu Geol. no. Z1, 180–187 (in Chinese with English abstract).
Ciobanu, C., Cook, N., Utsunomiya, S., Kogagwa, M., Green, L., Gilbert, S., Wade, B., 2012. Gold-telluride nanoparticles revealed in arsenic-free pyrite. Am. Mineral. 97, 1515–1518.
Clark, C., Grguric, B., Mumm, A.S., 2004. Genetic implications of pyrite chemistry from the Palaeoproterozoic Olary Domain and overlying Neoproterozoic Adelaidean sequences, northeastern South Australia. Ore Geol. Rev. 25 (3), 237–257.
Cook, N.J., 1996. Mineralogy of the sulphide deposits at Sulitjelma, northern Norway. Ore Geol. Rev. 11 (5), 303–338.
Cook, N.J., Ciobanu, C.L., Pring, A., Skinner, W., Shimizu, M., Danyushevsky, L., Saini-Eidukat, B., Melcher, F., 2009. Trace and minor elements in sphalerite: A LA-ICPMS study. Geochim. Cosmochim. Acta 73 (16), 4761–4791.
Cugerone, A., Cenki-Tok, B., Chauvet, A., Le Goff, E., Bailly, L., Alard, O., Allard, M., 2018. Relationships between the occurrence of accessory Ge-minerals and sphalerite in Variscan Pb-Zn deposits of the Bossost anticlinorium, French Pyrenean Axial Zone: Chemistry, microstructures and ore-deposit setting. Ore Geol. Rev. 95, 1–19.
Danyushevsky, L., Robinson, P., Gilbert, S., Norman, M., Large, R., McGoldrick, P., Shelley, M., 2011. Routine quantitative multi-element analysis of sulphide minerals by laser ablation ICP-MS: Standard development and consideration of matrix effects. Geochemistry Exploration Environment Analysis 11, 51–60.
Di Benedetto, F., Bernardini, G.P., Costagliola, P., Plant, D., Vaughan, D.J., 2005. Compositional zoning in sphalerite crystals. Am. Mineral. 90 (8–9), 1384–1392.
Einaudi, M. T., Meinert, L. D., Newberry, R. J., and Skinner, B. J., 1981, Skarn Deposits, Seventy-Fifth Anniversary Volume, Society of Economic Geologists, p. 0.
Feng, Y., Zhang, Y., Xie, Y., Shao, Y., Lai, C., 2020. Pyrite geochemistry and metallogenic implications of Gutaishan Au deposit in Jiangnan Orogen, South China. Ore Geol. Rev. 117, 103298.
Fernández, F.G.M., Both, R.A., Mangas, J., Arribas, A., 2000. Metallogenesis of Zn-Pb Carbonate-Hosted Mineralization in the Southeastern Region of the Picos de Europa (Central Northern Spain) Province, geologic fluid inclusion, and stable isotope studies. Econ. Geol. 95 (1), 19–40.
Fournier, R.O., 1999. Hydrothermal processes related to movement of fluid from plastic into brittle rock in the magmatic-epithermal environment. Econ. Geol. 94 (8), 1193–1211.
Frenzel, M., Hirsch, T., Gutzmer, J., 2016. Gallium, germanium, indium, and other trace and minor elements in sphalerite as a function of deposit type — A meta-analysis. Ore Geol. Rev. 76, 52–78.
Gagnevin, D., Menuge, J.F., Kronz, A., Barrie, C., Boyce, A.J., 2014. Minor elements in Layered Sphalerite as a Record of Fluid Origin, Mixing, and Crystallization in the Navan Zn-Pb Ore Deposit, Ireland*. Econ. Geol. 109 (6), 1513–1528.
George, L., Cook, N., Ciobanu, C., Wade, B., 2015. Trace and minor elements in galena: a reconnaissance LA-ICP-MS study. Am. Mineral. 100, 548–569.
Gong, H.T., Qi, Y.Q., Gao, J.F., Lv, C., Min, K., 2020. Source and Ore-forming Process of the Qixiashan Lead-zinc Ore Deposit, Jiangsu Province. Evidences from S-C-O Isotopes 39 (04), 779–793 (in Chinese with English abstract).
Gottesmann, W., Kampe, A., 2007. Zn/Cd ratios in calcsilicate-hosted sphalerite ores at Tumurtijn-ovoo, Mongolia. Geochemistry 67 (4), 323–328.
Grant, H.L.J., Hannington, M.D., Petersen, S., Frische, M., Fuchs, S.H., 2018. Constraints on the behavior of trace elements in the actively-forming TAG deposit, Mid-Atlantic Ridge, based on LA-ICP-MS analyses of pyrite. Chem. Geol. 498, 45–71.
Guan, J.P., Wei, F.B., Sun, G.X., Huang, J.P., Wang, L.J., 2015. Zircon U-Pb dating of intermediate-acid intrusive rocks in the middle section of Ningzhen district and their metallogenic implications. Geotecton. Metallog. 2, 344–354 (in Chinese with English abstract).
Gui, C.J., 2012. Mineral Deposit Genetic Study on the Qixiashan Pb-Zn Deposit in Nanjing. Nanjing University, Jiangsu Province, China, pp. 1–56 (in Chinese with English abstract).
Gui, C.J., Jing, S., Sun, G.C., 2015. Deep Prospecting Breakthrough of the Qixiashan Lead-Zinc Ore District in Nanjing and its Enlightenment. J. Geol. 39 (01), 91–98 (in Chinese with English abstract).
Guo, X.S., Xiao, Z.M., Ou, Y.J., Lu, Q.X., 1985. On the genesis of the qixishan lead-zinc ore deposit in Nanjing. Mineral. Deposita no. 01, 11–21 (in Chinese with English abstract).
Hedenquist, J.W., Lowenstern, J.B., 1994. The role of magmas in the formation of hydrothermal ore deposits. Nature 370 (6490), 519–527.
Huston, D.L., Sie, S.H., Suter, G.F., Cooke, D.R., Both, R.A., 1995. Trace elements in sulfide minerals from eastern Australian volcanic-hosted massive sulfide deposits; Part I, Proton microprobe analyses of pyrite, chalcopyrite, and sphalerite, and Part II, Selenium levels in pyrite; comparison with delta 34 S values and implications for the source of sulfur in volcanogenic hydrothermal systems. Econ. Geol. 90 (5), 1167–1196.
Large, R.R., Maslennikov, V.V., Robert, F.O., Danyushevsky, L.V., Chang, Z., 2007. Multistage sedimentary and metamorphic origin of pyrite and gold in the Giant Sukhoi Log deposit, Lena Gold Province, Russia. Econ. Geol. 102 (7), 1233–1267.
Large, R.R., Danyushevsky, L., Hollit, C., Maslennikov, V., Meffre, S., Gilbert, S., Bull, S., Scott, R., Emsbo, P., Thomas, H., Singh, B., Foster, J., 2009. Gold and Trace Element Zonation in Pyrite using a Laser Imaging Technique: Implications for the timing of Gold in Orogenic and Carlin-style Sediment-Hosted Deposits. Econ. Geol. 104 (5), 635–668.
Large, R.R., Mukherjee, I., Gregory, D.D., Steadman, J.A., Maslennikov, V.V., Meffre, S., 2017. Ocean and Atmosphere Geochemical Proxies Derived from Trace elements in Marine Pyrite: Implications for Ore Genesis in Sedimentary Basins. Econ. Geol. 112 (2), 423–450.

Large, R.R., Mukherjee, I., Gregory, D., Steadman, J., Corkrey, R., Danyushevsky, L.V., 2019. Atmosphere oxygen cycling through the Proterozoic and Phanerozoic. Mineral. Deposita 54 (4), 485–506.
Li, Z., Ye, L., Hu, Y., Wei, C., Huang, Z., Yang, Y., Danyushevsky, L., 2020. Trace elements in sulfides from the Maozu Pb-Zn deposit, Yunnan Province, China: Implications for trace-element incorporation mechanisms and ore genesis. Am. Mineral. 105 (11), 1734–1751.
Liu, S. H., 1999, Interpretation of Gravity and Magnetic Characteristics of the Qixiashan Pb-Zn Polymetal Deposit, Nanjing and discussion on its genesis, Contributions to Geology and Mineral Resources Research, v. 23, no. 1, p. 72–78.(in Chinese with English abstract).
Liu, Y.J., Cao, L.M., Li, Z.L., Wang, H.N., Chu, T.Q., Zhang, J.R., 1984. Element Geochemistry. Science Press, Beijing, pp. 1–548 (p.:(in Chinese).
Lockington, J.A., Cook, N.J., Ciobanu, C.L., 2014. Trace and minor elements in sphalerite from metamorphosed sulphide deposits. Mineral. Petrol. 108 (6), 873–890.
Loftus-Hills, G., Solomon, M., 1967. Cobalt, nickel and selenium in sulphides as indicators of ore genesis. Mineral. Deposita 2 (3), 228–242.
Mao, J.R., Zhao, S.L., 1990. Chemical evolution of magma in batholith of Nanjing-Zhenjiang Mountain. J. Nanjing Inst. Geol. Chin. Acad. Geol. Sci. 01, 15–28 (in Chinese with English abstract).
Mao, J., Pirajno, F., Cook, N., 2011a. Mesozoic metallogeny in East China and corresponding geodynamic settings — an introduction to the special issue. Ore Geol. Rev. 43 (1), 1–7.
Mao, J., Wang, Y., Lehmann, B., Yu, J., Du, A., Mei, Y., Li, Y., Zang, W., Stein, H.J., Zhou, T., 2006. Molybdenite Re–Os and albite $^{40}Ar/^{39}Ar$ dating of Cu–Au–Mo and magnetite porphyry systems in the Yangtze River valley and metallogenic implications. Ore Geol. Rev. 29 (3), 307–324.
Mao, J., Zhang, J., Pirajno, F., Ishiyama, D., Su, H., Guo, C., Chen, Y., 2011b. Porphyry Cu–Au–Mo–epithermal Ag–Pb–Zn–distal hydrothermal au deposits in the Dexing area, Jiangxi province, East China—A linked ore system. Ore Geol. Rev. 43 (1), 203–216.
Mao, Z., Cheng, Y., Liu, J., Yuan, S., Wu, S., Xiang, X., Luo, X., 2013. Geology and molybdenite Re–Os age of the Dahutang granite-related veinlets-disseminated tungsten ore field in the Jiangxin Province, China. Ore Geol. Rev. 53, 422–433.
Maslennikov, V.V., Maslennikova, S.P., Large, R.R., Danyushevsky, L.V., 2009. Study of Trace Element Zonation in Vent Chimneys from the Silurian Yaman-Kasy Volcanic-Hosted massive Sulfide Deposit (Southern Urals, Russia) using Laser Ablation-Inductively coupled Plasma Mass Spectrometry (LA-ICPMS). Econ. Geol. 104 (8), 1111–1141.
Meinert, L.D., 1987. Skarn zonation and fluid evolution in the Groundhog Mine, Central Mining district, New Mexico. Econ. Geol. 82 (3), 523–545.
Migdisov, A.A., Zezin, D., Williams-Jones, A.E., 2011. An experimental study of Cobalt (II) complexation in Cl^- and H_2S^-bearing hydrothermal solutions. Geochim. Cosmochim. Acta 75 (14), 4065–4079.
Nadoll, P., Angerer, T., Mauk, J.L., French, D., Walshe, J., 2014. The chemistry of hydrothermal magnetite: A review. Ore Geol. Rev. 61, 1–32.
Qi, Y., Hu, R., Gao, J., Leng, C., Gao, W., Gong, H., 2022. Trace and minor elements in sulfides from the Lengshuikeng Ag–Pb–Zn deposit, South China: A LA–ICP–MS study. Ore Geol. Rev. 141, 104663.
Reich, M., Deditius, A., Chryssoulis, S., Li, J.-W., Ma, C.-Q., Parada, M.A., Barra, F., Mittermayr, F., 2013. Pyrite as a record of hydrothermal fluid evolution in a porphyry copper system: A SIMS/EMPA trace element study. Geochim. Cosmochim. Acta 104, 42–62.
Roedder, E., 1968. The non-colloidal origin of 'colloform' textures in sphalerite ores. Econ. Geol. 63 (5), 451–471.
Román, N., Reich, M., Leisen, M., Morata, D., Barra, F., Deditius, A.P., 2019. Geochemical and micro-textural fingerprints of boiling in pyrite. Geochim. Cosmochim. Acta 246, 60–85.
Shimizu, T., Morishita, Y., 2012. Petrography, chemistry, and near-infrared MICROTHERMOMETRY of indium-bearing sphalerite from the TOYOHA polymetallic deposit, Japan. Econ. Geol. 107 (4), 723–735.
Sillitoe, R.H., 2010. Porphyry Copper Systems*. Econ. Geol. 105 (1), 3–41.
Sun, X.-J., Ni, P., Yang, Y.-L., Qin, H., Chen, H., Gui, C.-J., Jing, S., 2018. Formation of the Qixiashan Pb–Zn deposit in Middle-lower Yangtze River Valley, eastern China: Insights from fluid inclusions and in situ LA-ICP-MS sulfur isotope data. J. Geochem. Explor. 192, 45–59.
Sun, Y., Ma, C., Liu, Y., 2014. The latest Yanshanian magmatic and metallogenic events in the middle-lower Yangtze River belt: evidence from the Ningzhen region. Chin. Sci. Bull. 58 (34), 4308–4318.
Sun, X.J., Ni, P., Chi, Z., Yang, Y.L., Jing, S., Wang, G.G., 2019. The feature and evolution of ore-forming fluid of Qixiashan Pb-Zn deposit, Nanjing: constraints from fluid inclusion and H-O isotope. Acta Petrol. Sin. 35 (12), 3749–3762 (in Chinese with English abstract).
Sun, X., Ni, P., Yang, Y., Chi, Z., Jing, S., 2020. Constraints on the Genesis of the Qixiashan Pb-Zn Deposit, Nanjing: evidence from Sulfide Trace Element Geochemistry. J. Earth Sci. 31 (2), 287–297.
Thomas, H.V., Large, R.R., Bull, S.W., Maslennikov, V., Berry, R.F., Fraser, R., Froud, S., Moye, R., 2011. Pyrite and Pyrrhotite Textures and Composition in Sediments, Laminated Quartz Veins, and Reefs at Bendigo Gold Mine, Australia: Insights for Ore Genesis. Econ. Geol. 106 (1), 1–31.
Velásquez, G., Béziat, D., Salvi, S., Siebenaller, L., Borisova, A.Y., Pokrovski, G.S., De Parseval, P., 2014. Formation and Deformation of Pyrite and Implications for Gold Mineralization in the El Callao District, Venezuela. Econ. Geol. 109 (2), 457–486.
Wang, S.X., Zhou, H., 1993. Geological explanation of the geophysical and geochemical data on qixiashan lead, zinc, and silver mine. J. Geol. 017 (002), 107–113 (in Chinese with English Abstract).
Wang, C.M., Deng, J., Shouting, Z., Chunji, X.U.E., Yang, L., Qingfei, W., Sun, X., 2010. Sediment-hosted Pb-Zn Deposits in Southwest Sanjiang Tethys and Kangdian Area on the Western Margin of Yangtze Craton. Acta Geol. Sin. v, 84.
Wang, X.L., Zeng, J.N., Ma, C.Q., Li, X.F., Wu, Y.F., Lu, S.F., 2014. Zircon U-Pb dating of Yanshanian intrusive rocks in Ningzhen District, Jiangsu: the chronology evidence for a new stage of petrogenesis and metallogeny in the middle and lower reaches of Yangtze River. Earth Sci. Front. 21 (06), 289–301 (in Chinese with English abstract).
Wei, X.L., Jing, S., Sun, X.J., 2019. Geological characteristics and genesis of the Qixiashan lead-zinc deposit, Nanjing. J. Geol. 43 (04), 573–583 (in Chinese with English abstract).
Wei, C., Ye, L., Huang, Z., Hu, Y., Wang, H., 2021. In situ trace elements and S isotope systematics for growth zoning in sphalerite from MVT deposits: a case study of Nayongzhi, South China. Mineral. Mag. 85 (3), 364–378.
Wilkinson, J., Shaw, H., Herrington, R., 2000. Post-magmatic hydrothermal circulation and the origin of base metal mineralization, Cornwall, UK. J. Geol. Soc. 157, 589–600.
Williams-Jones, A.E., Samson, I.M., Ault, K.M., Gagnon, J.E., Fryer, B.J., 2010. The Genesis of Distal Zinc Skarns: evidence from the Mochito Deposit, Honduras. Econ. Geol. 105 (8), 1411–1440.
Wu, S.H., 2016. The Metallogenic Mechanism of Distal Contact Pb-Zn-ag Vines in Shizhuyuan Ore District, Hunan Province, China. China University of Geosciences, Beijing, pp. 1–109 (in Chinese with English abstract).
Wu, S.H., Mao, J.W., Xie, G.Q., Geng, J.Z., Xiong, B.K., 2015. Geology, geochronology, and Hf isotope geochemistry of the Longtougang skarn and hydrothermal vein Cu–Zn deposit, North Wuyi area, southeastern China. Ore Geol. Rev. 70, 136–150.
Xie, S.C., Yin, H.F., 1997. Biometallogenesis of Pb-Zn-Ag polymetallic deposit of Qixiashan in Nanjing. Geol. J. China Univ. 3 (2), 10 (in Chinese with English abstract).
Xu, Z.F., Zeng, Z.H., 2006. Discussions on relationship between mineralization and magmatism in Qixiashan Pb-Zn-Ag ore deposit of Nanjing: Jiangsu. Geology 030 (003), 177–182 (in Chinese with English abstract).
Ye, L., Cook, N.J., Ciobanu, C.L., Yuping, L., Qian, Z., Tiegeng, L., Wei, G., Yulong, Y., Danyushevskiy, L., 2011. Trace and minor elements in sphalerite from base metal deposits in South China: A LA-ICPMS study. Ore Geol. Rev. 39 (4), 188–217.
Ye, L., Gao, W., Yang, Y.L., Liu, T.G., Peng, S.S., 2012. Trace elements in sphalerite in Laochang Pb-Zn polymetallic deposit, Lancang, Yunnan Province. Acta Petrol. Sin. 28 (05), 1362–1372 (in Chinese with English abstract).
Ye, L., Li, Z. L., Hu, Y. S., Huang, Z. L., Fan, H. F., and Leonid, D., 2016, Trace elements in sulfide from the Tianbaoshan Pb-Zn deposit , Sichuan Province, China: a LA-ICPMS study: Acta Petrol. Sin., v. 32, no. 11, p. 3377–3393.in (Chinese with English abstract).
Yuan, M.-W., Li, S.-R., Li, C.-L., Santosh, M., Alam, M., Zeng, Y.-J., 2018. Geochemical and isotopic composition of auriferous pyrite from the Yongxin gold deposit, Central Asian Orogenic Belt: Implication for ore genesis. Ore Geol. Rev. 93, 255–267.
Zeng, J.N., Li, J.W., Chen, J.H., Lu, J.P., 2013. SHRIMP zircon U-Pb dating of Anjishan intrusive rocks in Ningzhen District, Jiangsu, and its geological significance. Earth Sci. 38 (01), 57–67 (in Chinese with English abstract).
Zhang, Q., 1987. Differentiating the genetic types of Pb-Zn deposits using trace element mapping of galena and sphalerite. Geol. Geochem. no. 09, 64–66 (in Chinese).
Zhang, M.C., 2015. Research on Metallization of the Qixiashan Lead-Zinc-Silver Polymetallic Deposit, Jiangsu Province, [ChinaDoctor]. China University of Geosciences, Beijing, pp. 1–222 (in Chinese with English abstract).
Zhang, Q., Liu, Z.H., Zhan, X.Z., Shao, S.X., 2003. Specialization of ore deposit types and minerals for enrichment of indium. Mineral Deposits no. 03, 309–316 (in Chinese with English abstract).
Zhang, M.C., Chen, R.Y., Ye, T.Z., Li, J.C., Lv, Z.C., He, X., Chen, H., Yao, L., 2017. Genetic study on the Qixiashan Pb-Zn polymetallic deposit in Jiangsu Province: Evidence from fluid inclusions and H-O-S-Pb isotopes. Acta Petrol. Sin. 33 (11), 3453–3470 (in Chinese with English abstract).
Zhang, M.C., Chen, R.Y., Li, J.C., Li, Y.S., Yao, L., Chen, H., Lai, S.H., Wang, T., 2019. Carbon, oxygen and strontium isotope geochemical characteristics of the Qixiashan Pb-Zn polymetallic deposit, Jiangsu Province, and their indication significance. Geol. Bull. Chin. 38 (09), 1529–1542 (in Chinese with English abstract).
Zhao, H.-X., Frimmel, H.E., Jiang, S.-Y., Dai, B.-Z., 2011. LA-ICP-MS trace element analysis of pyrite from the Xiaoqinling gold district, China: Implications for ore genesis. Ore Geol. Rev. 43 (1), 142–153.
Zhou, T.F., Wang, S.W., Yuan, F., Fan, Y., Zhang, D.Y., Chang, Y.F., White, N.C., 2016. Magmatism and related mineralization of the intracontinental porphyry deposits in the Middle-Lower Yangtze River Valley Metallogenic Belt. Acta Petrol. Sin. 32 (2), 271–288.
Zhu, X.Q., Zhang, Q., He, Y.L., Zhu, C.H., 2006. Relationships betweenindium and tin, zinc and lead in ore-forming fluid from the indiumrich and-poor deposits in China. Geochimica no. 01, 6–12 (in Chinese with English abstract).